PERGAMON

Journal of Structural Geology 22 (2000) 91–104

JOURNAL OF STRUCTURAL GEOLOGY

www.elsevier.nl/locate/jstrugeo

# Texture analysis of a recrystallized quartzite using electron diffraction in the scanning electron microscope

F. Heidelbach [a,*], K. Kunze [b], H.-R. Wenk [c]

[a] *Bayerisches Geoinstitut, Universität Bayreuth, D-95440 Bayreuth, Germany*
[b] *Geologisches Institut, ETH Zürich, Zürich, Switzerland*
[c] *Department of Geology and Geophysics, University of California, Berkeley, CA 94720, USA*

Received 14 January 1997; accepted 23 June 1999

**Abstract**

The microstructure and crystallographic preferred orientation (texture) of a recrystallized quartzite from the Bergell Alps was quantitatively investigated using automated indexing of electron backscattered patterns (EBSP). The results are displayed in orientation maps of the microstructure and orientation as well as misorientation distribution functions. The orientation distribution function derived from EBSP compares excellently with texture data derived from independent neutron diffraction experiments. The misorientation distribution function of next neighbors reveals strong maxima for small angle grain boundaries (subgrain boundaries) and the Dauphiné twin correlation. The Dauphiné twins, which are generally not detectable optically, are not correlated with specific maxima in the orientation distribution function. Their origin and their role during recrystallization is discussed. During recrystallization no other preferred high angle misorientations developed. The frequent occurrence of small angle grain boundaries indicates progressive subgrain rotation as a recrystallization mechanism. © 1999 Elsevier Science Ltd. All rights reserved.

## 1. Introduction

Although recrystallization is widespread in metamorphic quartzites, there are relatively few studies of the influence of recrystallization on the development of crystallographic preferred orientation. The separate textures of old relic grains (or porphyroclasts) and recrystallized grains in natural quartz tectonites were mostly investigated in mylonites with cross-girdle or double maxima patterns of the quartz *c*-axes (Ransom, 1971; Bell and Etheridge, 1976; Marjoribanks, 1976; Law et al., 1984; Law, 1986). The preferred orientation of recrystallized grains in these cases generally differed only in details from the texture of relic grains. In small circle textures, however, recrystallized grains formed a crossed-girdle pattern (Bell and Etheridge, 1976; Saha, 1989; Kirschner and Teyssier, 1991; Takeshita et al., 1999), that is, the recrystallization apparently produced new orientations with *c*-axes in the direction of the intermediate fabric direction. The change in texture from old to new grains has been interpreted in two ways:

1. The kinematic framework changed during deformation and dynamic recrystallization and this caused the change in preferred orientation (Kirschner and Teyssier, 1991, 1992).
2. The preferred orientation of the old grains is a residual texture, which consisted only of those grains least likely to recrystallize (Hippertt and Borba, 1992).

In a few studies (Ransom, 1971; Bell and Etheridge, 1976; Marjoribanks, 1976; Law et al., 1984; Law, 1986) the angles between the *c*-axes of adjacent old and new grains were investigated. The observed misorientation patterns were very similar in all of these studies, showing a high concentration of misorientation angles between 20° and 50°. Law and coworkers (1984,

* Corresponding author.
*E-mail address:* Florian.Heidelbach@uni-bayreuth.de (F. Heidelbach).

0191-8141/00/$ - see front matter © 1999 Elsevier Science Ltd. All rights reserved.
PII: S0191-8141(99)00125-X

1986) also calculated the rotation of the *c*-axis relative to the sample co-ordinates, and found that the *c*-axes of the new grains tended to rotate away from the macroscopic *Z* (direction of maximum finite shortening) towards the macroscopic *X* (direction of maximum finite elongation). The misorientation angle of *c*-axes in recrystallized quartzites from the Lepontine Alps was determined in an AVA ('Achsenverteilungsanalyse') study by Wenk (1965). There was no obvious correlation between neighboring orientations, although a general trend to larger orientation domains, defined by clusters of grains with similar orientation, was found within the microstructure. The influence of extensive grain boundary migration on the texture was documented by Jessell (1987) who distinguished growing and shrinking grains by characteristic microstructures of the grain boundaries in a recrystallized quartzite. The *c*-axes of apparently growing grains were predominantly oriented in the foliation, perpendicular to the lineation. Lloyd and Freeman (1991, 1994) studied the orientations of subgrains and recrystallized grains within one quartz porphyroclast using SEM electron channeling patterns (ECP) and interpreted them in terms of different slip systems active during dynamic recrystallization.

Recrystallization in quartzites has been simulated by introducing subgrain formation and grain boundary migration into computer models of deformation (Jessell, 1988a, b; Jessell and Lister, 1990; Wenk et al., 1997; Takeshita et al., 1999). A critical step in these calculations is the assumption as to which grains (or orientations) will grow; in other words, which have the lowest dislocation densities. This is in turn dependent on the plasticity theory used to model the deformation: under conditions of homogeneous strain (Taylor, 1938; Jessell and Lister, 1990) grains in 'soft' orientations will accumulate fewer dislocations, whereas under conditions of homogeneous stress (Sachs, 1928) grains in 'hard' orientations will have low dislocation densities because they do not deform appreciably (Karato, 1987). The influence of these grains on the texture is then solely dependent on the grain boundary migration rate. The self-consistent deformation model (Wenk et al., 1989) allows some heterogeneity of stress and strain. In the case of pure shear and simple shear, simulations of quartz deformation display a maximum of *c*-axes in the intermediate sample direction for the most highly deformed grains. This is a texture often encountered in naturally recrystallized quartzites (Price, 1985).

In the present study a recently developed technique of texture measurement (orientation imaging microscopy, Adams et al., 1993) was used to investigate the microstructure and texture of a recrystallized quartzite. With this method it is possible to reconstruct the spatial distribution of orientations, which is particularly interesting in recrystallized samples, where local orientation relationships may be important. The results are displayed in form of grain maps of the microstructure and the misorientation distribution functions (MDF).

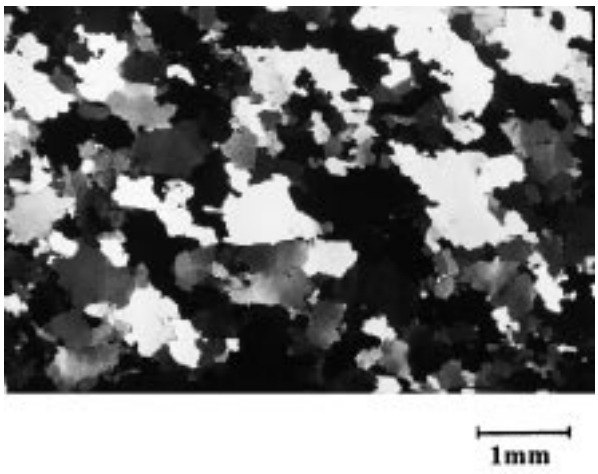


Fig. 1. Transmitted light micrograph (crossed polarizers) of sample BRG420.

## 2. Sample description

The studied sample, BRG420, is a recrystallized quartzite that was taken from a metasedimentary sequence in the upper part of the Suretta nappe in the northern Bergell Alps (Switzerland). The quartzites are probably of Triassic sedimentary age and were deformed during the Alpine orogeny at upper greenschist to amphibolite grade conditions in the Miocene (Wenk, 1973). The sample has a well-developed macroscopic foliation dipping to the northeast and an east-plunging lineation, which is mostly parallel to the local fold axis orientation. Besides quartz, the sample contains only a few muscovite grains that define the foliation. The microstructure (Fig. 1) is characterized by large grains (100–500 μm mean diameter) with some undulatory extinction and subgrain boundaries. The subgrain size is often fairly large (up to 50 μm) and the shapes vary from equant to elongated. The grain boundaries are mostly serrated and uneven. The grain shapes are often elongated at a high angle to the foliation. The microstructure indicates a high degree of grain boundary mobility with micas completely enclosed in quartz grains, concave and convex shaped grain boundaries and 'orientation families' of amoeba-like shapes (Urai et al., 1986).

This sample was chosen for this study for two reasons. Firstly, it was expected to show characteristics of a completely recrystallized fabric, i.e. that features developing during recrystallization, and particularly

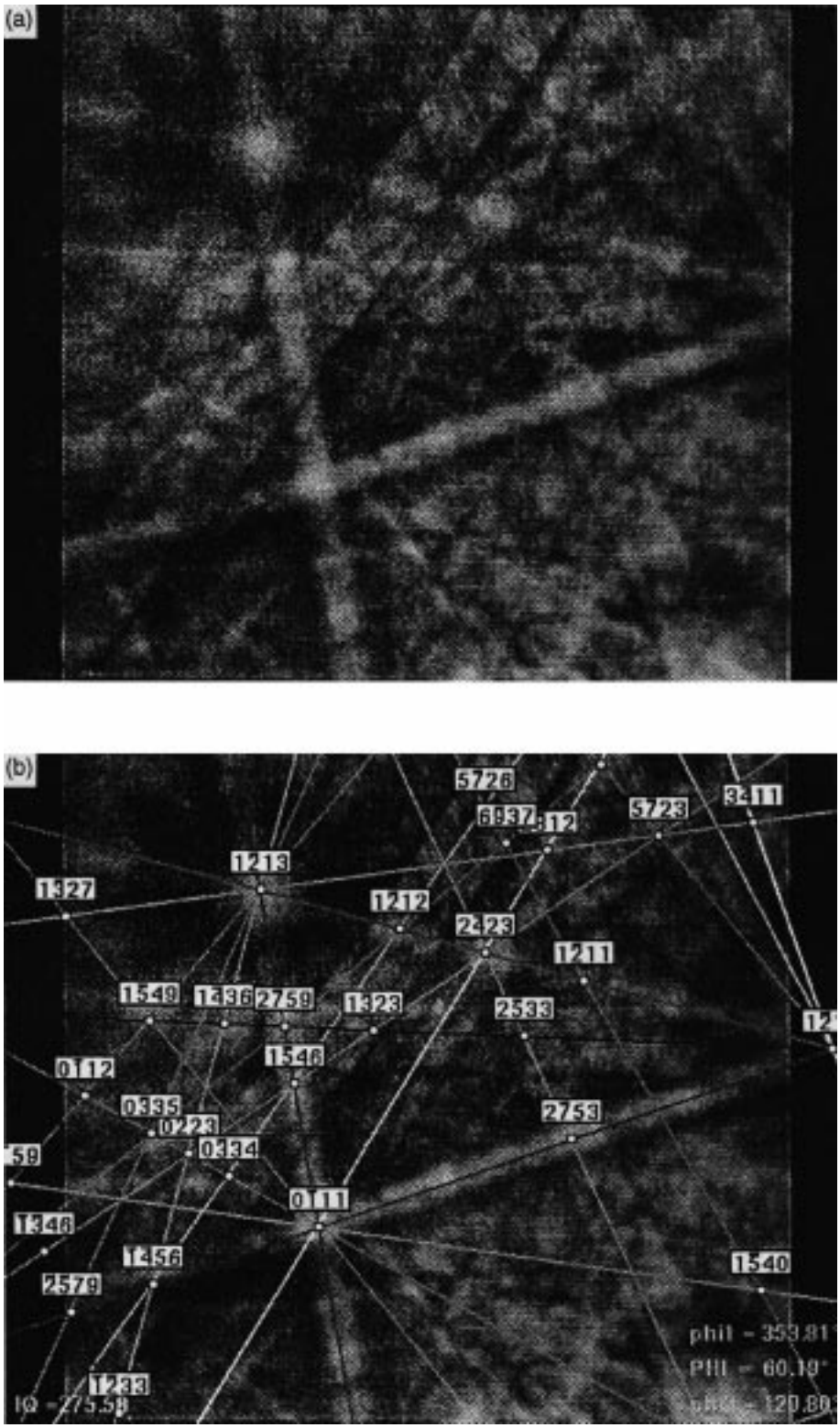


Fig. 2. Example of an EBSP pattern of quartz; (a) after image processing (frame averaging and background subtraction), (b) after indexing procedure.

grain boundary migration (e.g. preferred misorientations, orientation correlations) would be especially pronounced. Secondly, the sample was well suited as a test case for the application of orientation imaging microscopy because of the fairly simple microstructure and the good quality of the EBSP patterns. Also the sample shows a texture typical of recrystallized quartzites with *c*-axes forming a characteristic asymmetric maximum at high angles to the lineation and in the foliation plane (Helming et al., 1994).

## 3. Experimental technique

Although electron backscattering patterns (EBSP) have been described from studies with focussed electron beams since the early 1930s (Von Meibom and Rupp, 1933), their use for orientation determination in the SEM has been pointed out only in the past two decades (Dingley, 1981, 1984). The EBSP are generated by multiple scattering of the electrons within the crystal structure (Reimer, 1985) and are the backscattered equivalent of the classical Kikuchi patterns observed in transmission electron microscopy (Kikuchi, 1928). The patterns consist of a series of bands each of which corresponds to a certain lattice plane $\{hkl\}$ (Fig. 2). The width of the bands is inversely proportional to the lattice plane spacing and can be used, together with the angle between the bands, to index the diffraction pattern and to determine the crystal orientation for a known crystal lattice.

In this study, automated aquisition and analysis of EBSP were used as introduced by Adams et al. (1993) and extended for trigonal crystal symmetry by Kunze et al. (1993, 1994). This so-called orientation imaging microscopy (OIM) uses an automated stage to move the sample in a gridwise fashion underneath the focussed electron beam. At each point the electron backscattering pattern (which arises instantaneously) is detected with a phosphorus screen mounted in front of a video camera. The video image is digitally processed (image averaging and background subtraction) and the diffraction bands are recognized using a Hough transform of the image (Illingworth and Kittler, 1988). The set of interplanar angles derived from the position of the bands is compared with a reference list of angles for the particular crystal structure to find the best solution for the orientation. Fig. 2 shows a processed EBSP and the best fit indexing solution. The fully automated procedure allows for rapid measurement of a large number of points on the specimen (about one per second).

A problem in indexing quartz arises from the hexagonal pseudosymmetry around the *c*-axis (60° rotation), which corresponds to the Dauphiné twin relationship. Patterns that are related by this pseudosymmetry can only be distinguished by the recognition of the reflection bands with true trigonal symmetry, meaning that the intensity difference between positive and negative forms (e.g. reflections of the *r* and *z* planes) had to be recognized and incorporated into the indexing routine for each pattern in our measurement. With this addition (see also Kunze et al., 1993 for details) a reliable indexing of the trigonal symmetry was feasible.

## 4. Sample preparation and measurement

The sample was prepared according to a method introduced by Fynn and Powell (1979). A slab of the sample, cut parallel to the lineation and perpendicular to the foliation was mechanically ground with a final particle size of the medium of 0.25 μm and then polished with a high pH silica solution (SYTON) for about 12 h in order to remove surface damage. The setup of the polishing machine did not allow for the preparation of thin sections so that the image of the measured area for comparison with the measurement had to be taken in reflected light. The sample was not carbon coated because this would have diminished the intensity of the backscattered diffraction patterns. Charging effects in the SEM were reduced by using a low accelerating voltage (8 keV). The measured area was about 1 $cm^2$ in size and scanned in a hexagonal grid with 50 μm stepwidth resulting in 46 316 data points. After the EBSP measurement, the surface was slightly etched with HF. The etch exposed grain boundaries as well as Dauphiné and Brazil twins (e.g. Frondel, 1945) and also increases the contrast of differently oriented grains. The etching also had a side effect whereby a hexagonal pattern of etch marks is visible in some areas of the sample, corresponding to the grid used in the automated measurement. The etch enhanced the contrast originating from contamination or damage at spots where the beam was focussed.

A cube of 1 $cm^3$ was taken from the same sample adjacent to the measured surface for neutron diffraction experiments. These experiments are described in more detail elsewhere (Schäfer et al., 1992; Helming et al., 1994).

## 5. Calculation of misorientations

A misorientation between two crystal orientations can be expressed mathematically as the product of the two orientation matrices:

$$\Delta g_{AB}(i,k) = g_C^i g_A g_B^{-1} g_C^k$$

where $\Delta g_{AB}$ is the misorientation matrix, $g_A$, $g_B$ are the respective orientation matrices of the crystals A

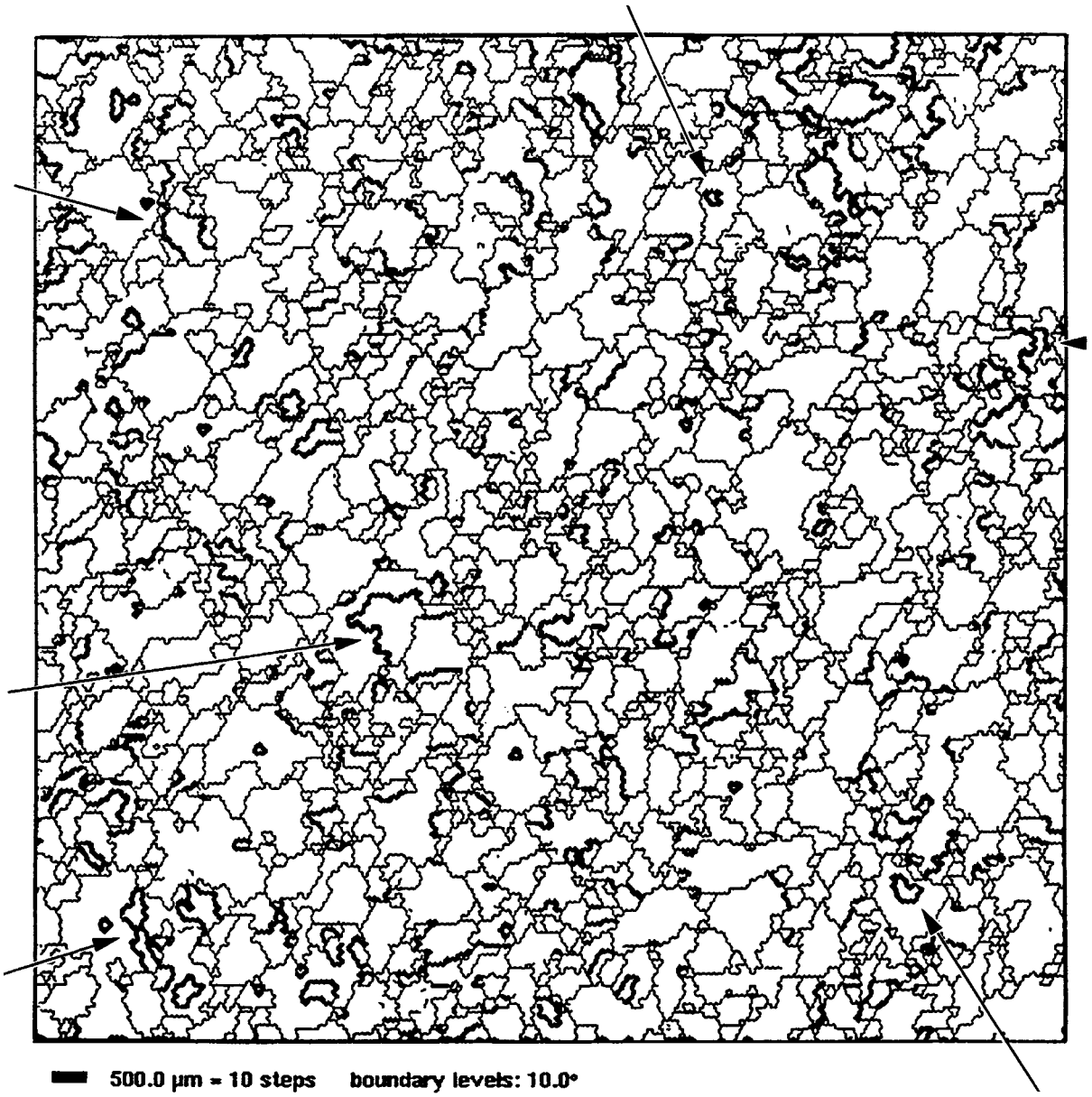


Fig. 3. Grain map of measured area in sample BRG420; grain boundaries with $\omega > 10^\circ$ are indicated by thin lines, Dauphiné twin boundaries ($60^\circ\langle 0001\rangle \pm 2.5^\circ$) are indicated by thick lines; arrows point to areas for comparison with the reflected light micrograph in Fig. 4.

and B and $g_C$ represents the rotation matrix of the crystal symmetry with $i$, $k$ symmetry elements. The misorientation matrix can be transformed into the three Euler angles relating the two crystal orientations or into a rotation axis/angle pair. In this study we chose rotation axis/angle pairs for the representation of misorientations because they are a clear and easy way to visualize a misorientation. Two differing co-ordinate systems can be brought to coincidence by a rotation $\omega$ about a particular rotation axis, which is the direction that is identical in both co-ordinate systems. This representation is traditionally applied in crystallography to twins where the axis is a rational lattice direction $[uvw]$ and the angle a simple fraction of $2\pi$, e.g. Dauphiné twins in quartz are represented by a $60^\circ$ (or $180^\circ$) rotation about $\langle 0001\rangle$. Crystals exhibit several equivalent misorientations due to their symmetry. In the case of trigonal crystals (rotation symmetry 32) there are six equivalent axis/angle pairs depending on which $a$-axes are brought into coincidence with each other. Each of these misorientations has a different rotation angle. The misorientation distribution functions (MDF) in this study are shown as distributions of rotations with the smallest possible rotation angle for each misorientation. The smallest among equivalent angles does not necessarily have a

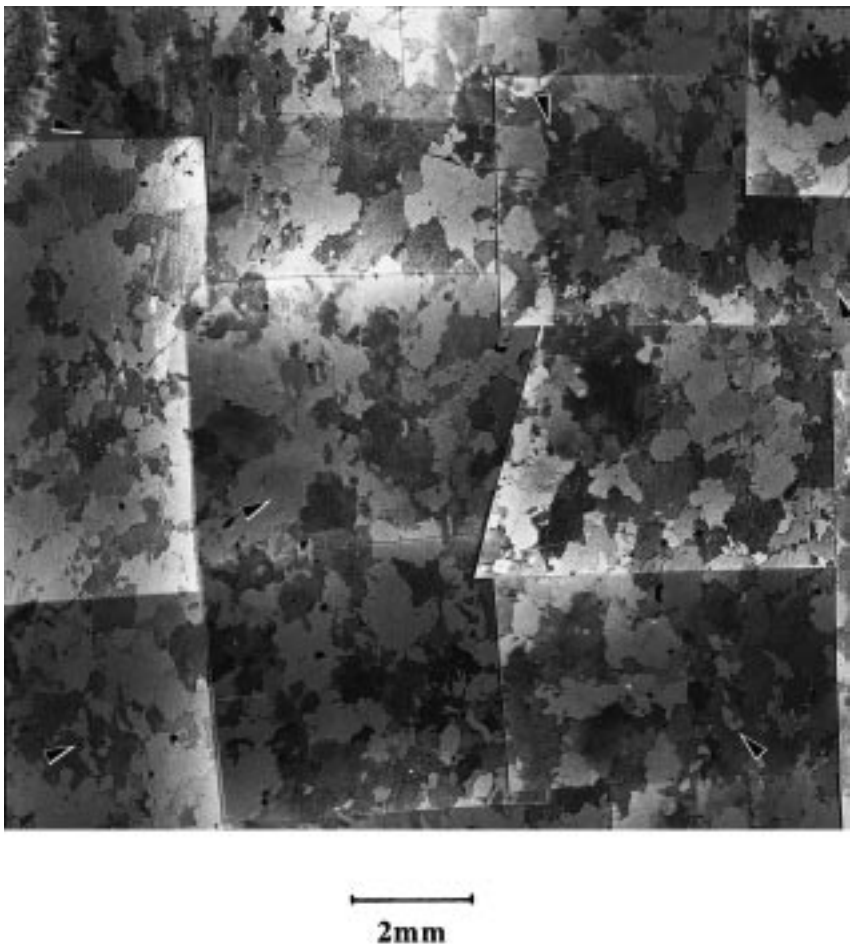


Fig. 4. Reflected light micrograph of measured area in sample BRG420; arrows point to areas easy to compare with grain map in Fig. 3.

particular physical meaning, but it is useful to identify and distinguish various types of misorientations (e.g. small and large angle grain boundaries, Σ boundaries (see Kronberg and Wilson, 1949; Mykura, 1979; Grimmer, 1980; McLaren, 1986)). The range of 'smallest' angles $\omega_{min}$ of a rotation matrix is determined by the symmetry of the two crystal systems. The maximum value of $\omega_{min}$ for trigonal crystals is 104.5°.

Misorientations can be displayed in the sample co-ordinate system as well as in the crystal co-ordinate system. The details of the calculation of the misorientation distribution function relative to both co-ordinate systems as well as the respective symmetries are described in the Appendix.

## 6. Results

### 6.1. Microstructures

Grain maps reproducing the microstructure of the sample are constructed from the data by analysis of the misorientations of nearest neighbor pairs of sample points on the measurement grid. In Fig. 3 misorientation angles exceeding 10° are represented by a light line segment between the respective points. Misorientations close to the Dauphiné twin relationship of a 60° rotation about ⟨0001⟩ (±2.5°) are highlighted by a thick line. The grain map compares well with a reflected light micrograph of the measured area (Fig. 4). In particular, the twin boundaries (thick boundaries in grain map), which were made visible by etching in the sample, can be easily identified in the image of the surface of the sample (see arrows in Figs. 3 and 4). The twins have mostly straight boundaries and often emerge from grain boundaries. Brazil twins, which cannot be distinguished with the EBSP method (Olesen and Schmidt, 1990), but should also be visible after etching, do not appear to be present in this sample.

### 6.2. Textures

As a test for the EBSP method of texture measure-

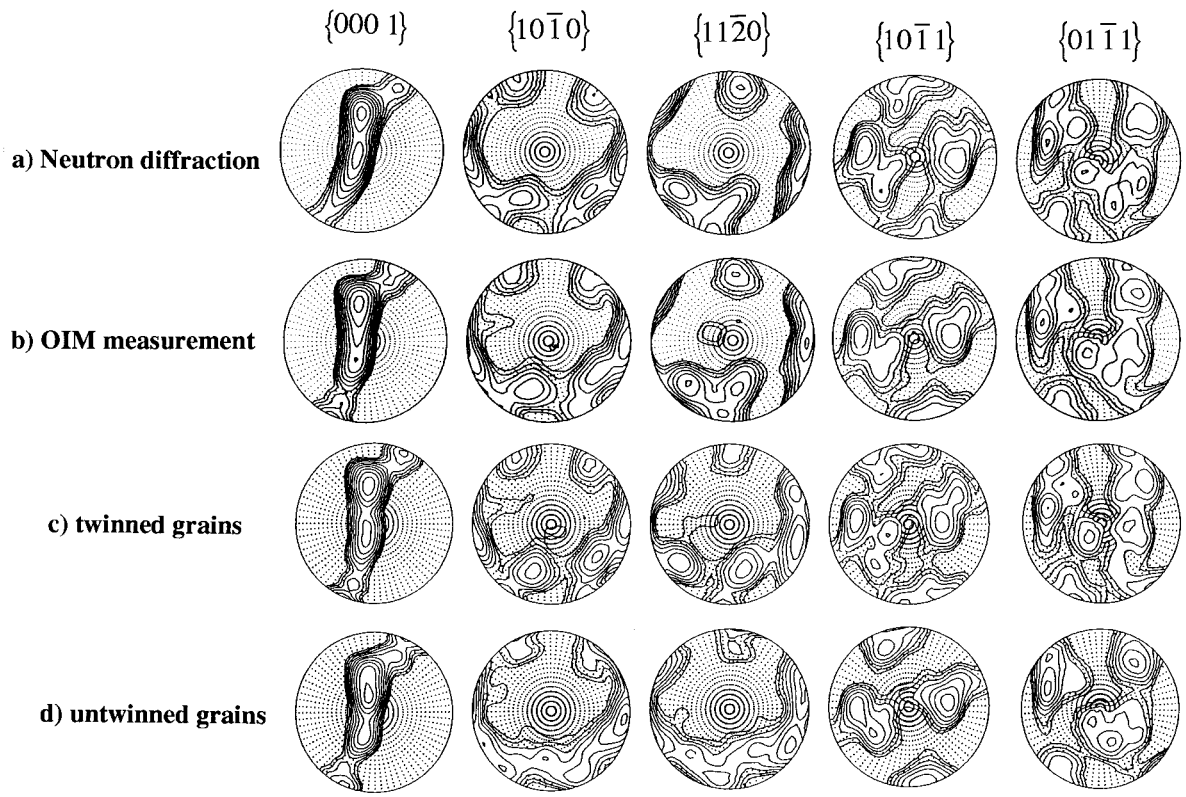


Fig. 5. Contoured pole figures for sample BRG420 from (a) neutron diffraction experiments and (b–d) OIM measurements: (b) all data; (c) only twinned grains; (d) only untwinned grains; equal area projections are perpendicular to the foliation (trace of foliation is horizontal) and parallel to the lineation (also horizontal); contours are at 0.5, 0.7, 1.0, 1.4, 2.0, 2.8, 4.0, 5.6, 8, 11.3 multiples of random distribution (m.r.d.), areas below 1 m.r.d. are dotted.

ment the data from the OIM measurement are compared with independent neutron diffraction data from the same specimen (Helming et al., 1994). Individual orientations from automatic EBSP measurements were first entered into $5 \times 5 \times 5$ degree ODF cells, and these ODF cells were then smoothed with a Gauss function of 10° FWHM (see Appendix). In the case of neutron diffraction the ODF was derived from pole figures with the WIMV algorithm. Then the pole figures were recalculated from the ODF. The pole figures derived from both techniques are very similar (Fig. 5a, b). In particular it should be noted that the pole figures for the positive and negative rhombohedral planes (*r* and *z*) are very similar in both measurements indicating that the true trigonal symmetry is correctly identified in the OIM measurement. The texture of the sample is best described as an asymmetric girdle of {0001} planes which is approximately perpendicular to the foliation and lineation. The highest concentration of {0001} forms an elongated maximum within the girdle, in the foliation plane and perpendicular to the lineation. The {11$\bar{2}$0} pole figures show a maximum concentration close to the lineation. This type of texture is typical for quartz mylonites which were subjected to ductile deformation and recrystallization (Schmid and Casey, 1986; Helming et al., 1994). In Fig. 5(c) and (d) the textures of grains with and without Dauphiné twins are shown: the pole figures for both types of

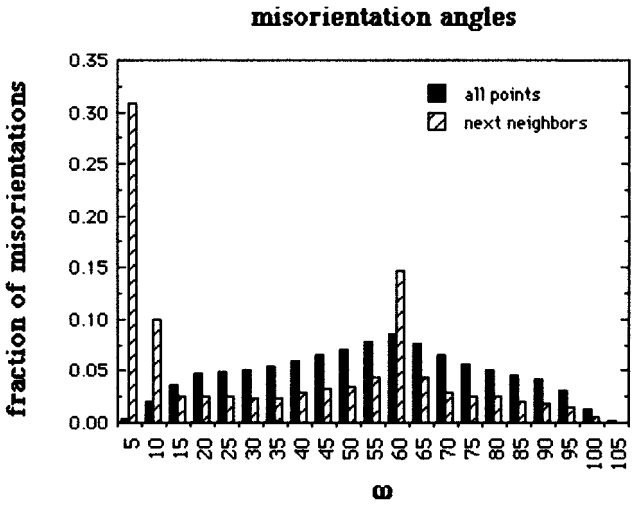


Fig. 6. Histogram of misorientation angle $\omega$ for misorientations between next neighbors and misorientation between all data points irrespective of their position in the measurement grid; frequencies are normalized to 1.

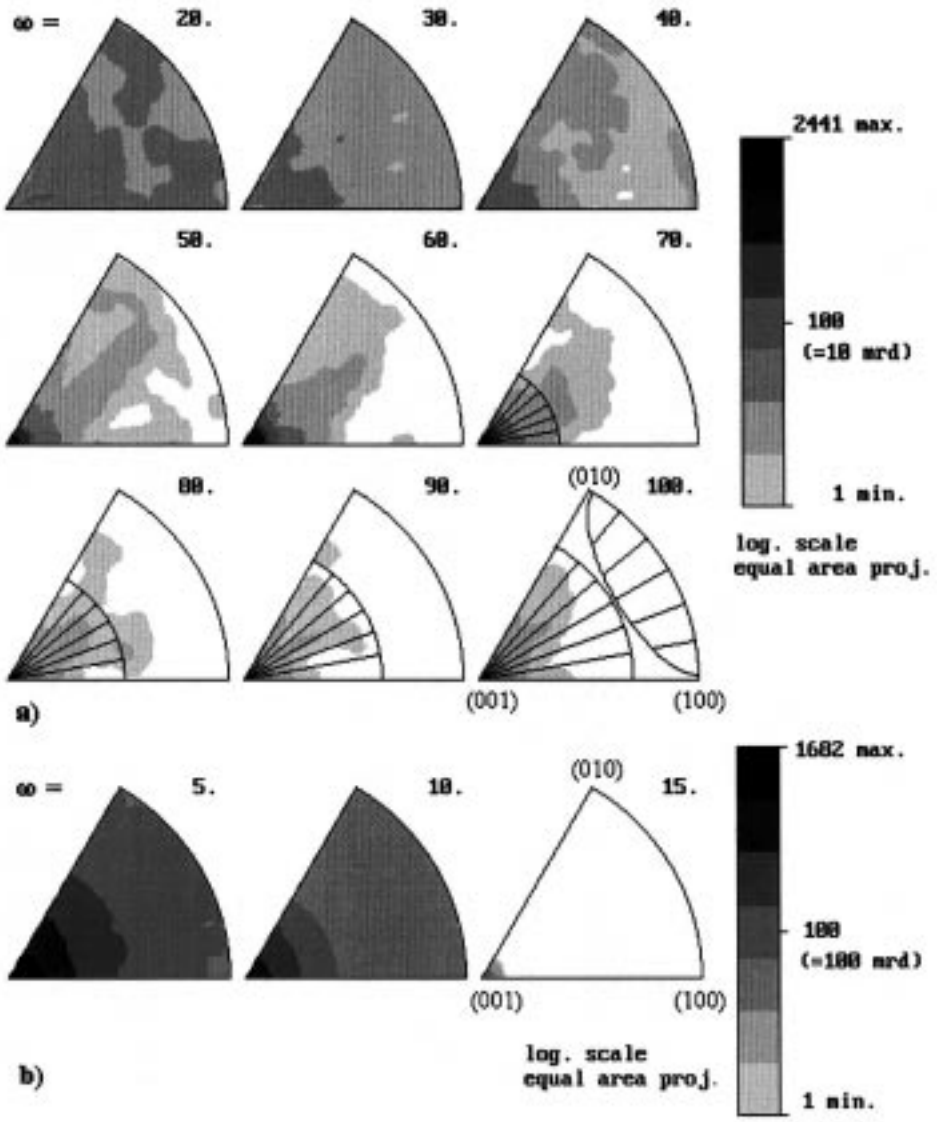


Fig. 7. Misorientation distribution function of next neighbors for sample BRG420 in crystal co-ordinates displayed in $\omega$-sections; (a) all misorientations with $\omega > 17.5^\circ$; (b) misorientations with $2.5 < \omega < 17.5^\circ$; areas outside the asymmetric (basic) region (see Appendix) are marked with radial lines.

grains are very similar suggesting that there is no preferential Dauphiné twinning of specific orientations.

### 6.3. Misorientations

The misorientation angles ($\omega$) between all next neighboring data points were calculated. Their distribution ('next neighbors') is compared to the distribution of misorientation angles between all data points irrespective of their position in the measuring grid ('all points') in Fig. 6. The latter gives the distribution of misorientation angles determined purely by the texture of the sample (Pospiech et al., 1993). Angles smaller than 2.5° were omitted in both calculations since such angles can result from inaccuracy in measuring the same orientation. The frequency of all misorientations increases steadily up to 60° and then decreases until the maximum angle of 104.5° is reached. The shape of this distribution can be explained by the volume of the elementary region of misorientation space, which increases up to 60° and then decreases towards the maximum angle. The histogram for next neighbor misorientations, on the other hand, shows two distinct maxima: a very high one at low angles (2.5–15°) and a smaller one at 60°.

The distribution of rotation axes in crystal space is displayed in Fig. 7, in sections of equal $\omega$. Because the number of small angle misorientation is very high the misorientation distribution functions were separated (Fig. 7a: $\omega > 17.5^\circ$, Fig. 7b: $\omega < 17.5^\circ$) in order to make the orientation of the rotation axes with high rotation angles visible. The maximum at 60° is concen-

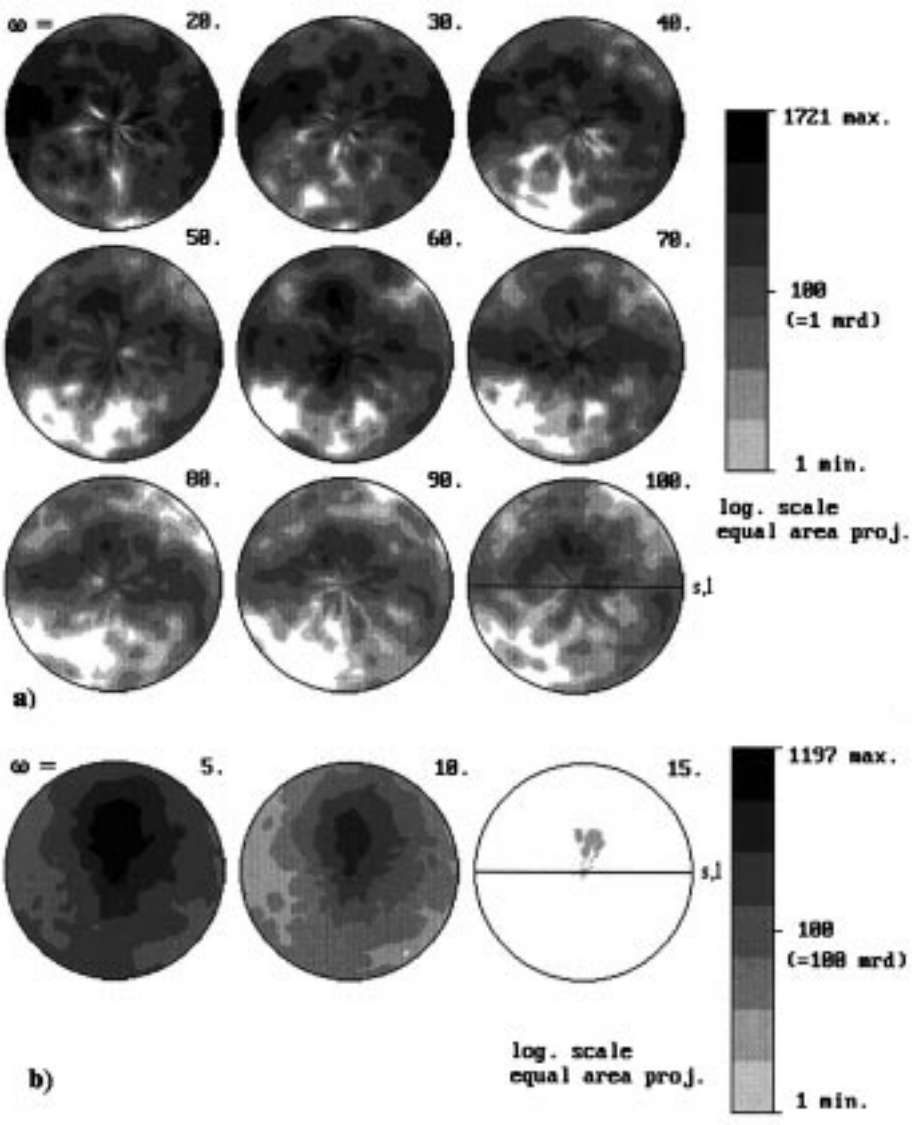


Fig. 8. Misorientation distribution function of next neighbors sample BRG420 in sample co-ordinates displayed in $\omega$-sections; (a) all misorientations with $\omega > 17.5^\circ$; (b) misorientations with $2.5 < \omega < 17.5^\circ$; equal area projections are perpendicular to the foliation (trace of foliation is horizontal) and parallel to the lineation (also horizontal).

trated very sharply in the *c*-axis direction representing the Dauphiné twins marked in the grain map (Fig. 3) by thick boundaries and visible in the micrograph (Fig. 4). Apart from this maximum at the twin position there are relatively few misorientations with angles lower than 40° and those are concentrated preferentially around the [0001] axis. Above 40° this maximum increases to a peak at 55° and also broadens towards the negative pole of the *m* plane. Generally there are low densities in the directions perpendicular to the *c*-axis. The small angle rotations (Fig. 7b) are distributed fairly evenly over the whole unit triangle with the maximum concentration close to [0001].

In Fig. 8 the distribution of the rotation axes relative to the sample co-ordinates (foliation and lineation) is shown in sections of different misorientation angle, $\omega$. As in Fig. 7 the misorientation distribution functions were calculated separately for rotations with $\omega > 17.5^\circ$ (Fig. 8a) and $\omega < 17.5^\circ$ (Fig. 8b). At low angles and at 60° the distribution is similar to the {0001} pole figure (Fig. 5). The second feature in this distribution is a great circle of misorientation axes, which is at an oblique angle to the foliation plane at low misorientation angles ($\omega = 20$–$40^\circ$) and almost parallel to it at higher misorientation angles ($\omega > 40^\circ$).

## 7. Discussion

The results described above suggest that the OIM method is a valid method to measure textures in quartzites. The excellent match of neutron and electron dif-

fraction data indicates that the texture in this sample is very homogeneous, considering that the number of grains measured in the neutron diffraction experiment is about 35 times larger than in the OIM measurement, assuming an average grainsize of 300 μm. The texture of this sample is typical for recrystallized quartzites (Price, 1985).

The very high number of small angle grain boundaries ($\omega = 2.5$–$17.5^\circ$) reflects the local heterogeneity of orientations within one grain. Because of the relatively large stepwidth (50 μm) of the measurement grid, these orientation differences are due both to subgrains (dislocation walls) as well as continuous lattice bending (undulatory extinction). The predominant orientation of the rotation axes close to the *c*-axis has to be interpreted with caution for two reasons. First, at low rotation angles, the absolute orientation difference between rotation axes is much smaller than at larger rotation angles. Second, the higher concentration in direction of the *c*-axis may be purely due to the strong *c*-axis texture of the sample. Similar orientation differences between subgrains in a recrystallized porphyroclast were interpreted by Lloyd and Freeman (1991, 1994) in terms of slip systems active during the deformation. The direction of the rotation axis, however, becomes less significant for small rotation angles (it is undefined for $\omega = 0$, see Appendix), hence there appears to be a high uncertainty for this kind of analysis.

The second characteristic feature of the misorientation distribution is the maximum at the Dauphiné twin position. The rotation connected with this twin (60° around the *c*-axis) does not change the position of the crystal axes, but reverses the polarity of the *a*-axes and exchanges positive and negative forms (e.g. *r* and *z* rhombohedral planes). Besides the Brazil twin, the Dauphiné twin is the most common twin in quartz and has been observed abundantly in many varieties of quartz. There have, however, been very few reports of the occurrence of Dauphiné or other twins in metamorphic rocks (Trommsdorff and Wenk, 1963), mostly because they are not detectable in conventional transmitted light microscopy. With the more widespread use of electron backscattering techniques in the SEM they have been reported more often in deformed rocks (e.g. Lloyd et al., 1992; Mainprice et al., 1993). Dauphiné twins are generated at the transition from hexagonal β-quartz to trigonal α-quartz (573°C at 1 atm; Frondel, 1962), but can also be formed due to mechanical or thermal stresses (Schubnikow and Zinserling, 1932; Zinserling and Schubnikow, 1933; Frondel, 1945). Near the α–β transition temperature Dauphiné twin boundaries are very mobile (Van Tendeloo et al., 1976; Barber and Wenk, 1991). Preferential growth of one twin orientation (piezocrescence) has been found to correlate with the different ability to store elastic strain energy (Thomas and Wooster, 1951).

Due to the low temperature history of this sample, the Dauphiné twins cannot have formed at the α–β-quartz phase transition. An origin due to mechanical stress or growth under stress would make an orientation dependance of the twin formation likely, but the orientation distributions for twinned quartz and the whole sample are very similar (see Fig. 5b–d). Tullis and Tullis (1972) experimentally produced twins in compression, which caused a preferential alignment of the *r*-planes relative to the *z*-planes perpendicular to the compression direction. A similar trend is visible in the pole figures (Fig. 5) where the *r*-planes have a maximum parallel to the foliation, whereas the *z*-planes do not show any concentration in that direction. It is therefore possible that the Dauphiné twinning contributed to the sharp difference between the pole figures of the *r*- and *z*-planes. In addition the generation of twins due to thermal stresses (i.e. during the cooling phase) seems to be a probable mechanism in this sample. The location of the twins at the grain boundaries as places of stress concentrations during cooling supports this interpretation.

The misorientation distribution of high angle grain boundaries ($> 17.5^\circ$) has generally high densities in the direction of the *c*-axis. Similar to the maximum of rotation axes at low angles, this may be due to the strong *c*-axis texture, which statistically produces a higher probability that rotation axes are parallel to the *c*-axis (texture dependent part of the MDF). The absence of any other strong discrete maxima in the misorientation distribution function suggests that the recrystallization process does not promote particular orientation correlations to develop. In the MDF relative to the sample co-ordinates there is some indication that rotation axes tend to align perpendicular to the foliation normal. It also shows that the orientation of the Dauphiné twins is controlled by crystallography and not by the sample framework.

The questions then arises as to if and how the twinning and the recrystallization in this sample are related to each other. There are no signs of twins of different grains being connected to each other or new grains forming at twin boundaries, which might be expected, if an already twinned crystal recrystallizes. The microstructures and misorientations suggest that twinning postdated recrystallization.

## 8. Conclusions

The present study represents one of the first applications (see also Pearson et al., 1997) of orientation imaging microscopy (OIM) to a quartzite. A natural quartz texture typically developing during dynamic

recrystallization is presented and investigated. The results demonstrate the suitability of the technique for texture measurements. The misorientation distribution function for next neighbors shows only little variation besides a high concentration of low angle boundaries and a maximum at the Dauphiné twin position. The uniformity of the distribution of high angle grain boundaries indicates that there are no preferred misorientations developing during the recrystallization process. The low angle grain boundaries ($\omega = 2.5$–$17.5^\circ$) are due to subgrains and lattice bending. There were no indications that the twinning in this sample is related to the recrystallization process which has been observed in other materials, e.g. in copper (Haasen, 1992).

**Acknowledgements**

We would like to thank J. Pospiech and S. Matthies for their help with the analysis of single crystal orientation data. N.Ø. Olesen and N.H. Schmidt are thanked for their help with the sample preparation. The paper benefitted greatly from thorough reviews by G.E. Lloyd and an anonymous reviewer. This work has been supported through an IGPP grant for FH and HRW. The work has been supported through grants by IGPP–LANL, NSF and the Center for Materials Science at Los Alamos. The EBSP measurements were done at Brigham Young University through the courtesy of Prof. B. Adams.

## Appendix A

### *A.1. Calculation of the orientation distribution function (ODF)*

The orientation data measured with the OIM method consist of three Euler angles which represent discrete points in orientation space. A continuous orientation distribution function (ODF) can be calculated from these points by applying a Gaussian function to each data point (Matthies and Vinel, 1993). We used a Gaussian function of the form:

$$f(S, \omega) = N(S)\exp[S\cos(\omega)],$$

where $S$ is a measure of the sharpness of the peak, and $\omega$ is the orientation distance from the peak. The orientation distance corresponds to the smallest rotation angle between two orientations (Matthies et al., 1987) and represents the true angular distance between them. The width of the peak was determined by using full width at half maximum height (FWHM $= b$), which was defined as

$$b = 4\arcsin[\ln 2/(2S)]^{0.5}.$$

The FWHM of the Gaussian was $15^\circ$ for all ODFs calculated in this study.

### *A.2. Calculation of the misorientation distribution function (MDF)*

The spatial distribution of rotation axis/angle pairs can be represented either relative to the crystal co-ordinates or relative to the sample co-ordinates. In either representation the full MDF contains a number $n$ of equivalent axis/angle pairs for one misorientation matrix:

$$n = 2^* S_a^* S_b$$

where $S_a$ and $S_b$ are the number of symmetry elements in the respective co-ordinate system and the factor 2 arises from the assumption that the misorientation matrix is equivalent to its inverse (Sztwiertnia et al., 1990).

The misorientation space can therefore be divided into $n$ asymmetric basic regions, each of which contains the complete misorientation distribution. In the case of two trigonal crystals, $n$ equals 72 ($2 \times 6 \times 6$). The symmetrically equivalent misorientations relative to the crystal co-ordinate system were calculated by:

$$\Delta g_{AB}^{crystal}(i, k) = g_C^i g_A g_B^{-1} g_C^k \quad i, k = 1, 2, \ldots, 6$$

where $g_C$ are the rotation matrices of the crystal symmetry.

The inverse symmetry described above adds a mirror symmetry in the MDF so that only half the size of the regular unit triangle for each crystal system has to be shown. At higher rotation angles ($> 60^\circ$ for trigonal) the boundaries of the basic region in axis/angle space become curved surfaces. These surfaces have a fairly complicated shape in axis/angle space, but can easily be derived using Rodrigues parameters (Heinz and Neumann, 1991).

By calculating the misorientation $\Delta g$ between two orientations $g_A$ and $g_B$ the information about the misorientation relative to the sample co-ordinate system is lost. In order to display the MDF relative to the sample co-ordinates, this information has to be retrieved by multiplying the rotation axis with the inverse of one of the orientation matrices:

$$\mathbf{n}_s = g_A^{-1}\mathbf{n}_c$$

where $\mathbf{n}_s$ is the rotation axis relative to the sample co-ordinates and $\mathbf{n}_c$ is the same rotation axis relative to the crystal co-ordinates. The orientation matrix $g_A$ rotates the sample co-ordinates into the crystal co-ordinates, the inverse matrix $g_A^{-1}$ does the opposite. The symmetrically equivalent misorientations relative

to the sample frame are described by:

$$\Delta g_{AB}^{sample}(i,k) = g_A^{-1} g_C^i g_A g_B^{-1} g_C^k g_A \quad i,k = 1,2,\ \ldots\ ,6.$$

The misorientation distribution function therefore has triclinic–triclinic symmetry and has to be plotted in the full sphere of rotation axes and the full range of rotation angles (0–180°).

In the following section, the calculation of one misorientation axis/angle pair and its transformation into the MDF is outlined. The rotation angle $\omega$ can be derived from the misorientation matrix $\Delta g$ by:

$$\cos\omega = \frac{(w_{11} + w_{22} + w_{33}) - 1}{2}$$

where $w_{11}$, $w_{22}$, $w_{33}$ are the diagonal elements of the misorientation matrix $\Delta g$. In order to find the smallest rotation angle, $\Delta g$ is rotated by the crystal symmetry elements $g_C$. Once the misorientation matrix with the smallest rotation angle $\omega_{min}$ is found, the co-ordinates of the rotation axis are calculated according to:

$$r_1 = \frac{(w_{23} - w_{32})}{2{*}\sin(\omega_{min})} \quad r_2 = \frac{(w_{31} - w_{13})}{2{*}\sin(\omega_{min})} \quad r_3 = \frac{(w_{12} - w_{21})}{2{*}\sin(\omega_{min})}$$

where $w_{12}$, $w_{21}$, $w_{13}$, $w_{31}$, $w_{23}$ and $w_{32}$ are the off-diagonal elements of the misorientation matrix $\Delta g$, and $r_1$, $r_2$, $r_3$ are the Cartesian co-ordinates of the rotation axis in the crystal co-ordinate system. The rotation axis is then transferred into the basic region (by rotation with the appropriate crystal symmetry elements), in which the MDF is calculated. This procedure has been described by Sztwiertnia et al. (1990) for cubic crystal symmetries and has been adjusted accordingly for trigonal crystal symmetry in this study.

The MDF was calculated in one basic region in rotation axis/angle space, i.e. in the co-ordinates $\omega$, $\theta$, and $\psi$. A Gaussian was applied to each single misorientation and its original co-ordinates $\omega$, $\theta$, and $\psi$; the densities were then added into 5° by 5° by 5° volume elements in the axis/angle space taking into account the volume correction for each element. The Gaussian was of the form

$$f(\sigma,\chi) = N(\Delta g_n)\exp(-\chi^2/\sigma^2),$$

where $\Delta g_n$ is the misorientation, $\chi$ is the orientation distance from $\Delta g_n$ in steps of $\omega$, $\theta$ and $\psi$, and $\sigma$ defines the width of the Gaussian. The use of these co-ordinates for the definition of the Gaussian width instead of the true orientation distance (as for the ODF, see above) has some implications for the interpretation of the MDF diagrams. The volume of the axis/angle space increases with increasing rotation angle $\omega$. As a consequence, the true orientation distance between the center and the edge of the inverse pole figure for $\omega = 5°$ is much smaller than at $\omega = 60°$. Therefore, the effective width of the Gaussian used in the MDF calculation becomes smaller with smaller rotation angles. For example, at $\omega = 5°$ a change of 90° in $\theta$ represents 7.1° in orientation distance, whereas at $\omega = 60°$ the same increment corresponds to 82.8°. The distance $\omega$ (the misorientation angle) between two misorientations (in axis/angle parameters $\mathbf{n}_1$, $\omega_1$ and $\mathbf{n}_2$, $\omega_2$) can be calculated by:

$$\cos(\omega/2) = \cos(\omega_1/2)\cos(\omega_2/2) + (\mathbf{n}_1 \cdot \mathbf{n}_2)\sin(\omega_1/2)\sin(\omega_2/2)$$

(Matthies *et al.*, 1987). The Gaussian was used here despite this distortion because one goal of the study was to detect point maxima in the MDF (preferred misorientations) and the angular distance between them was of lesser importance.

In this study a Gaussian with $\sigma = 5°$ was used, which provided a continuous distribution and still preserved the main characteristics of the distributions. The resulting MDF was normalized so that

$$\int f(\Delta g)\, d\Delta g = 1$$

was satisfied (Pospiech *et al.*, 1986).

## References


Adams, B.L., Wright, S.I., Kunze, K., 1993. Orientation imaging: the emergence of a new microscopy. Metallurgical Transactions 24A, 819–833.

Barber, D.J., Wenk, H.R., 1991. Dauphiné twinning in deformed quartzites: Implications of an in situ TEM study of $\alpha$–$\beta$ phase transformation. Physics and Chemistry of Minerals 17, 492–502.

Bell, T.H., Etheridge, M.A., 1976. The deformation and recrystallization of quartz in a mylonite zone, central Australia. Tectonophysics 32, 235–267.

Dingley, D., 1981. A comparison of diffraction techniques in the SEM. Scanning Electron Microscopy IV, 273–286.

Dingley, D., 1984. Diffraction from sub-micron areas using electron backscattering in a scanning electron microscope. Scanning Electron Microscope II, 569–575.

Frondel, C., 1945. Secondary Dauphiné twinning in quartz. American Mineralogist 30, 447–460.

Frondel, C., 1962. Dana's System of Mineralogy. John Wiley, New York.

Fynn, G.W., Powell, W.J.A., 1979. The Cutting and Polishing of Electro-optical Materials. Adam Hilger, Bristol.

Grimmer, H., 1980. A unique description of the relative orientation of neighbouring grains. Acta Crystallographica A36, 382–389.

Haasen, P., 1992. Extended nucleation and growth to the recrystallization (rx) texture. Scripta Metallurgica et Materialia 27, 1477–1484.

Heinz, A., Neumann, P., 1991. Representation of orientation and disorientation data for cubic, hexagonal, tetragonal and orthorhombic crystals. Acta Crystallographica A47, 780–789.

Helming, K., Wenk, H.R., Choi, C.S., Schäfer, W., 1994. Description of quartz textures by components. Examples from metamorphic rocks. In: Bunge, H.-J., Siegesmund, S., Skrotzki,

W., Weber, K. (Eds.), Textures of Geological Materials. Deutsche Gesellschaft für Materialkunde, Oberursel, pp. 303–325.
Hippertt, J.F.M., Borba, R.P., 1992. Quartz *c*-axis fabrics differences between porphyroclasts and recrystallized grains: Discussion. Journal of Structural Geology 14, 627–630.
Illingworth, J., Kittler, J., 1988. A survey of the Hough transform. Computer Vision, Graphics and Image Processing 44, 87–116.
Jessell, M.W., Lister, G.S., 1990. A simulation of the temperature dependence of quartz fabrics. In: Knipe, R.J., Rutter, E.H. (Eds.), Deformation Mechanisms, Rheology and Tectonics. Geological Society Special Publication 54, pp. 353–362.
Jessell, M.W., 1987. Grain-boundary migration microstructures in a naturally deformed quartzite. Journal of Structural Geology 9, 1007–1014.
Jessell, M.W., 1988a. Simulation of fabric development in recrystallizing aggregates—I. Description of the model. Journal of Structural Geology 10, 771–778.
Jessell, M.W., 1988b. Simulation of fabric development in recrystallizing aggregates—II. Example model runs. Journal of Structural Geology 10, 779–793.
Karato, S.I., 1987. Seismic anisotropy due to lattice preferred orientation of minerals: kinematic or dynamic? In: Manghnani, M.H., Syono, Y. (Eds.), High-pressure Research in Mineral Physics. Geophysical Monograph 39, pp. 455–471.
Kikuchi, S., 1928. Diffraction of cathode rays by mica. Japanese Journal of Physics 5, 83–96.
Kirschner, D., Teyssier, C., 1991. Quartz *c*-axis fabrics differences between porphyroclasts and recrystallized grains. Journal of Structural Geology 13, 105–109.
Kirschner, D., Teyssier, C., 1992. Quartz *c*-axis fabrics differences between porphyroclasts and recrystallized grains: Reply. Journal of Structural Geology 14, 631–634.
Kronberg, M.L., Wilson, F.H., 1949. Secondary recrystallization in copper. Metals Transactions 185, 501–514.
Kunze, K., Adams, B.L., Heidelbach, F., Wenk, H.-R., 1993. Local microstructural investigations in recrystallized quartzite using orientation imaging microscopy. International Conference on Textures in Materials 10, Clausthal-Zellerfeld. Trans Tech Publications, pp. 1243–1249.
Kunze, K., Heidelbach, F., Wenk, H.-R., Adams, B.L., 1994. Orientation imaging microscopy of calcite rocks. In: Bunge, H.-J., Siegesmund, S., Skrotzki, W., Weber, K. (Eds.), Textures of Geological Materials. Deutsche Gesellschaft für Materialkunde, Oberursel, pp. 127–146.
Law, R.D., Knipe, R.J., Dayan, H., 1984. Strain path partitioning within thrust sheets: microstructural and petrofabric evidence from the Moine thrust zone at Loch Eriboll, northwest Scotland. Journal of Structural Geology 6, 477–497.
Law, R.D., 1986. Crystallographic fabrics and strain in quartzites, Brittany. Journal of Structural Geology 8, 493–515.
Lloyd, G.E., Freeman, B., 1991. SEM electron channelling analysis of dynamic recrystallization in a quartz grain. Journal of Structural Geology 13, 945–953.
Lloyd, G.E., Freeman, B., 1994. Dynamic recrystallization of quartz under greenschist conditions. Journal of Structural Geology 16, 867–881.
Lloyd, G.E., Law, R.D., Mainprice, D., Wheeler, J., 1992. Microstructural and crystal fabric evolution during shear zone formation. Journal of Structural Geology 14, 1079–1110.
Mainprice, D., Lloyd, G.E., Casey, M., 1993. Individual orientation measurements in quartz polycrystals—advantages and limitations for texture analysis and petrophysical property determination. Journal of Structural Geology 15, 1169–1187.
Marjoribanks, R.W., 1976. The relation between microfabric and strain in a progressively deformed quartzite sequence from central Australia. Tectonophysics 32, 269–293.
Matthies, S., Vinel, G.W., 1993. On some methodical developments concerning calculations performed directly in orientation space. International Conference on Textures in Materials 10, Clausthal-Zellerfeld. Trans Tech Publications, pp. 1641–1646.
Matthies, S., Vinel, G.W., Helming, K., 1987. Standard Distributions in Texture Analysis. Akademie Verlag, Berlin.
McLaren, A.C., 1986. Some speculations of the nature of high-angle grain boundaries in quartz rocks. In: Hobbs, B.E., Heard, H.C. (Eds.), Mineral and Rock Deformation: Laboratory Studies. Geophysical Monograph 36, pp. 233–245.
Mykura, H., 1979. A checklist of Cubic Coincidence Site Lattice Relations. In: Grain Boundary Structure and Kinetics. ASM Materials Science Seminar, pp. 445–456.
Olesen, N.Ø., Schmidt, N.H., 1990. The SEM/ECP technique applied on twinned quartz crystals. In: Knipe, R.J., Rutter, E.H. (Eds.), Deformation Mechanisms, Rheology and Tectonics. Geological Society Special Publication 54, pp. 369–373.
Pearson, A., Heidelbach, F., Wenk, H.R., 1997. Texture analysis of quartz in a granite mylonite by EBSP-orientation imaging microscopy. Textures and Microstructures 29, 185–199.
Pospiech, J., Sztwiertnia, K., Haessner, F., 1986. The misorientation distribution function. Textures and Microstructures 6, 201–215.
Pospiech, J., Lücke, K., Sztwiertnia, K., 1993. Orientation distribution and orientation correlation functions for the description of microstructures. Acta Metallurgica et Materialia 41, 305–321.
Price, G.P., 1985. Preferred orientations in quartzites. In: Wenk, H.R. (Ed.), Preferred Orientation in Deformed Minerals and Rocks: An Introduction to Modern Texture Analysis. Academic Press, Orlando, pp. 385–405.
Ransom, D.M., 1971. Host control of recrystallized quartz grains. Mineralogical Magazine 38, 83–88.
Reimer, L., 1985. Scanning Electron Microscopy. Springer-Verlag, Berlin.
Sachs, G., 1928. Zur Ableitung einer Fliessbedingung. Zeitschrift des Vereins deutscher Ingenieure 12, 134–136.
Saha, D., 1989. The Caledonian Skerrols Thrust, SW Scotland—microstructure and strain. Journal of Structural Geology 11, 553–568.
Schäfer, W., Jansen, E., Merz, P., Will, G., Wenk, H.R., 1992. Neutron diffraction texture investigation on deformed quartzites. Physica B 180–181, 1035–1038.
Schmid, S., Casey, M., 1986. Complete fabric analysis of some commonly observed quartz-*c*-axis patterns. In: Hobbs, B.E., Heard, H.C. (Eds.), Mineral and Rock Deformation: Laboratory Studies. Geophysical Monograph 36, pp. 263–286.
Schubnikow, A., Zinserling, K., 1932. Über die Schlag- und Druckfiguren und über die mechanischen Quarzzwillinge. Zeitschrift für Kristallographie 83, 243–264.
Sztwiertnia, K., Pospiech, J., Haessner, F., 1990. Reduction of misorientations between two cubic crystals into the base domain of axis–angle space. Textures and Microstructures 12, 233–242.
Takeshita, T., Wenk, H.R., Lebensohn, R., 1999. Development of preferred orientation and microstructure in sheared quartzite: comparison of natural and simulated data. Tectonophysics (in press).
Taylor, G.I., 1938. Plastic strain in metals. Journal of the Institute of Metals 62, 307–324.
Thomas, L.A., Wooster, W.A., 1951. Piezocrescence—the growth of Dauphiné twinning in quartz under stress. Proceedings of the Royal Society of London A208, 43–62.
Trommsdorff, V., Wenk, E., 1963. Diskussion eines Zwillingsgefüges durch Achsenverteilungsanalyse an Quarz eines Tessinergneises. Schweizerische Mineralogische und Petrographische Mitteilungen 43, 687–698.
Tullis, J., Tullis, T., 1972. Preferred orientation of quartz produced by mechanical Dauphiné twinning: Thermodynamics and axial experiments. In: Heard, H.C., Borg, I.Y., Carter, N.C., Raleigh,

C.B. (Eds.), Flow and Fracture of Rocks. Geophysical Monograph 16, pp. 67–82.

Urai, J.L., Means, W.D., Lister, G.S., 1986. Dynamic recrystallization in minerals. In: Hobbs, B.E., Heard, H.C. (Eds.), Mineral and Rock Deformation: Laboratory Studies. Geophysical Monograph 36, pp. 161–199.

Van Tendeloo, G., Van Landuyt, J., Amelinckx, S., 1976. The $\alpha \rightarrow \beta$ phase transition in quartz and $AlPO_4$ as studied by electron microscopy. Physica Status Solidi A33, 723–735.

Von Meibom, R., Rupp, E., 1933. Elektronenbeugung in weiten Winkeln. Zeitschrift der Physik 82, 690–696.

Wenk, H.R., Canova, G., Molinari, A., Kocks, U.F., 1989. Viscoplastic modeling of texture development in quartzite. Journal of Geophysical Research 94, 17895–17906.

Wenk, H.R., Canova, G., Brechet, Y., Flandin, L., 1997. A deformation-based model for recrystallization of anisotropic materials. Acta Materialia 45, 3283–3296.

Wenk, H.R., 1965. Gefügestudien an Quarzknauern und -lagen der Tessiner Kulmination. Schweizerische Mineralogische und Petrographische Mitteilungen 45, 467–515.

Wenk, H.R., 1973. The structure of the Bergell Alps. Eclogae Geologicae Helvetiae 66, 255–291.

Zinserling, K., Schubnikow, A., 1933. Über die Plastizität des Quarzes. Zeitschrift für Kristallographie 85, 454–461.